RSC Advances

PAPER

View Article Online
View Journal | View Issue

Cite this: *RSC Adv.*, 2024, **14**, 29344

Cobalt–zinc carbides embedded in N-doped porous carbon nanospheres as polysulfide mediators for efficient lithium–sulfur batteries†

Xiangyu Tan,‡[a] Jiajun Du,‡[c] Haitao Wu,[c] Xuyu Ma,[b] Chunbo Zhou,[d] Fangrong Zhou,[a] Caijin Fan,[e] Xueqin Xu,[d] Shaocong Hou *[b] and Xin Cai *[c]

Developing high-efficiency interlayer catalysts is a promising tactic for improving the cycling performance of rechargeable lithium–sulfur (Li–S) batteries. Herein, using the Prussian blue analogue as the precursor, cobalt–zinc carbide nanocrystal-embedded N-doped porous carbon (Co_3ZnC@NC) is synthesized *via* simple post-carbonization. The obtained Co_3ZnC@NC nanospheres exhibit a robust core–shell structure showing good conductivity, high porosity and available metal active sites, favoring the interfacial charge transfer and the electron transport upon electrochemical reactions. The results demonstrate that the Co_3ZnC@NC catalyst is quite suitable for boosting the adsorption and redox conversion kinetics of soluble polysulfides. When acting as the separator interlayer, Co_3ZnC@NC contributes to improved Li–S batteries with a high discharge specific capacity of 1659.8 mA h g^{-1} at 0.1C and superior cycling stability of over 250 cycles at 1.0C (high capacity retention of 84.1% after 100 cycles at 0.5C). Furthermore, the Co_3ZnC@NC-based battery can maintain a high discharge capacity of 734.0 mA h g^{-1} at 5.0C, along with delivering a stable reversible capacity of 805.4 mA h g^{-1} (~5 mA h cm^{-2}) after 50 cycles even under a high sulfur loading of 6.2 mg cm^{-2}. This study affords a viable way to construct highly dispersed bimetal/carbon composites for efficient catalysts and renewable energy devices.

Received 26th June 2024
Accepted 23rd August 2024

DOI: 10.1039/d4ra04657a

rsc.li/rsc-advances

1. Introduction

The ubiquitous application of numerous portable electronics and the continued success of plug-in electric vehicles have increasingly motivated the exploration of high-performance and safe electrochemical battery systems.[1] In addition to traditional ion-intercalation batteries, rechargeable lithium–sulfur (Li–S) batteries have become one of the preferred solutions for advancing current energy storage devices.[2] Based on the electrocatalytic sulfur chemistry, Li–S batteries possess outstanding theoretical energy density (2600 W h kg^{-1}) and high theoretical specific capacity (1675 mA h g^{-1}), along with the merits of naturally abundant sulfur and eco-friendliness.[3,4] However, today's Li–S electrochemistry is inherently plagued by several drawbacks, including the poor inherent conductivity of the active sulfur and the insoluble lithium sulfide, the volumetric expansion of the sulfur cathode, and the notorious shuttling of soluble polysulfide lithium (Li_2S_x, LiPSs).[5,6] More importantly, the lithium metal anode has high reactivity and often tends to form unstable structures on its surface during prolonged electrochemical reactions.[7] Moreover, the shuttling of LiPSs could cause unnecessary side reactions on the lithium metal surface and induce the formation of more lithium dendrites, seriously affecting the long-term cycling stability, especially the safety of Li–S batteries.[8]

To inhibit the shuttling effect of LiPSs for improved Li–S batteries, tremendous efforts have been made to elucidate the reaction mechanism of Li–S electrochemistry.[9] Thus, designing suitable high-activity electrocatalysts has become a primary option that can speed up the slow reaction kinetics of lithium polysulfides involving a complex multi-electron transfer process.[10] As an indispensable part of the electrochemical energy device, the separator could play a crucial role in modulating the complicated "solid–liquid–solid" interfacial reactions during lithium storage, thus largely impacting the performance of Li–S batteries.[11] Accordingly, modifying commercial separators with functional interlayer electrocatalysts has been a feasible strategy for promoting battery performance.[12] Those functional separators can generally mitigate LiPS shuttling by trapping the dissolvable LiPSs at the cathode side and

[a]*Power Science Research Institute of Yunnan Power Grid Co., Ltd., Kunming 650214, China*

[b]*School of Electrical Engineering and Automation, Wuhan University, Wuhan 430072, China. E-mail: sc.hou@whu.edu.cn*

[c]*College of Materials and Energy, South China Agricultural University, Guangzhou 510642, China. E-mail: caixin2015@scau.edu.cn*

[d]*Qujing Power Supply Bureau of Yunnan Power Grid Co., Ltd., Qujing 655099, China*

[e]*State Key Laboratory of HVDC, Electric Power Research Institute, CSG, Guangzhou, 510080, China*

† Electronic supplementary information (ESI) available. See DOI: https://doi.org/10.1039/d4ra04657a

‡ Xiangyu Tan and Jiajun Du contributed equally to this work.

effectively reducing the corrosion of the lithium anode.[13] Among diverse interlayer catalysts, various porous carbon materials have been adopted to obtain functional separators, limiting the shuttle of polysulfides by physically blocking the LiPSs with abundant and appropriate pores.[14] Taking advantage of electronegative heteroatom (*e.g.* N, S, and P) doping, the physical adsorption and binding ability of the carbon surface toward the LiPSs can be increased.[15] However, the chemical affinity and electrochemical properties of most carbon catalysts toward sulfur electrocatalysis are still restricted, leaving sufficient room to improve the cycling capacities and the long-term stability of corresponding Li–S batteries.[16]

To address these issues, polar metal compounds (*e.g.* sulfides, nitrides, oxides and phosphides of non-precious metals) with strong chemical affinity and abundant electroactive sites are introduced as catalysts for boosting the sluggish redox conversion of LiPSs at the multiphase interfaces.[17–19] By rationally hybridizing metal compounds with porous carbon matrix, desirable catalysts with good conductivity, high selective permeability and excellent electrocatalytic activities can be achieved.[20–23] Such hybridized catalysts are promising to use fully the synergistic effects between the porous carbon nanostructure and the metal active sites, which considerably accelerates the adsorption and catalytic conversion of LiPSs during reversible battery reactions.[24,25] Intriguingly, transition metal carbides have attracted much attention in (electro-)catalytic fields due to their electroactivity, prominent electronic conductivity, high stability and good compatibility with carbon supports.[26–28] By constructing desired transition metal carbide-based hybrid catalysts, one major challenge is to ensure homogeneously dispersed and sufficient metal active sites in the carbon matrix.[29] Moreover, the different valence changes in the metal centers are often conducive to manipulating the charge transfer as well as the adsorption/desorption behavior between the active sites and the LiPS intermediates, which ultimately influence the redox kinetics of Li–S electrochemical reactions.[30,31] In early 2016, Wang *et al.* hybridized exfoliated-metal carbide ($Ti_3C_2T_x$) nanosheets with mesoporous carbon to host sulfur. Profiting from the effective trapping of sulfur and polysulfides by metal carbides, the sulfur cathode contributed to improved Li–S batteries with a discharge capacity of 1225.8 mA h g^{-1} and stable cycling of over 300 cycles at 0.5C.[32] Zhang *et al.* used nitrogen-doped carbon-supported Co_3Mo_3C to modify the commercial separator. The results demonstrated that bimetallic Co_3Mo_3C could provide more binding sites for polysulfide adsorption and catalysis compared with monometallic Mo_2C, thus leading to highly stable Li–S batteries with greatly increased sulfur utilization.[33] Hong *et al.* proposed $Ni_3ZnC_{0.7}$/Ni/NCNTs-functionalized separators for high-performance Li–S batteries with excellent rate capabilities. The study illustrated the advantageous properties of the bimetal carbides with sulfophilic Ni sites and lithophilic Zn sites to regulate the redox kinetics of polysulfides.[34] Despite this encouraging progress, it is still essential to develop high-efficiency bimetal carbide-based interlayer catalysts through simpler, low cost, and scalable syntheses to better increase sulfur utilization toward practical Li–S batteries.[35]

In consideration of the above, in this work, we designed nitrogen-doped porous carbon-encapsulated cobalt–zinc carbides (Co_3ZnC@NC) nanospheres through a simple one-pot synthesis. The Co_3ZnC@NC composite was derived from the post-carbonization of the Prussian blue analogue precursor. Benefiting from the core–shell structure that comprises highly dispersed bimetal carbide nanocrystals and thin N-doped carbon shells, Co_3ZnC@NC was endowed with hierarchical pores, good conductivity and abundant metal catalytic sites. Experimental results demonstrated the key role of Co_3ZnC@NC in boosting the adsorption and reversible catalytic conversion of LiPSs during electrochemical reactions. By modifying the commercial polypropylene separator with Co_3ZnC@NC, corresponding rechargeable Li–S batteries achieved high discharge capacities (1144.6 mA h g^{-1} at 0.5C), superior cyclic stability (long cycling of over 250 cycles at 1.0C) and good high-rate performance (734.0 mA h g^{-1} at 5.0C), showing inhibited shuttling of polysulfides upon charge/discharge cycling.

2. Experimental

2.1 Synthesis of materials

2.1.1 Synthesis of Co_3ZnC@NC. Note that 1.3293 g of potassium–cobalt cyanide was added to 100 mL of deionized water and labeled as solution A. A total of 0.2920 g of $Co(NO_3)_2 \cdot 6H_2O$ and 1.4875 g of $Zn(NO_3)_2 \cdot 6H_2O$ were added to 100 mL of deionized water to form solution B. Then, solution B was slowly dropped into solution A under an agitated state. The mixture underwent continuous stirring for 10 min at room temperature and was then left to age for 24 h. After centrifugation, pink precipitates were obtained, washed, and further dried in a vacuum at 60 °C to form the pink precursor of the Prussian blue analogue (PBA). The precursor was then placed in a tube furnace for post carbonization at 700 °C for 1 h under the protection of the N_2 atmosphere at a heating rate of 3 °C min^{-1}. After cooling to room temperature, the powder sample was collected and labeled as Co_3ZnC@NC.

2.1.2 Preparation of the modified separators. The interlayer catalyst (Co_3ZnC@NC), the conductive carbon black (Super P) and the polymeric binder (polyvinylidene fluoride, PVDF) were weighed at a mass ratio of 8 : 1 : 1, respectively, while *N*-methylpyrrolidone (NMP) was used as the solvent and stirred for 12 h to obtain a uniform mixture. Then, the resulting slurry was coated onto one side of the commercial separator (Celgard 2500) by applying the doctor blading method. The modified separators were then dried overnight in a vacuum oven at 60 °C, generating the Co_3ZnC@NC/PP separators. Typically, Co_3ZnC@NC/PP separators were cut into 19 mm discs with a catalyst loading amount of approximately 0.8 mg cm^{-2}. In comparison, the Super P modified separator (Super P/PP) was prepared according to the same procedures without incorporating Co_3ZnC@NC.

2.2 Preparation of the electrodes

2.2.1 Preparation of the sulfur cathode. The carbon/sulfur composites were prepared using the hot melting method.

Sublimed sulfur and Ketjen black (ECP-200L) were ground, evenly mixed in an agate mortar with a mass ratio of 3 : 1 for 15 min, and then placed into a tube furnace. The powder was heated at 155 °C for 12 h under N_2 atmosphere and further sublimated at 200 °C for 30 min at a heating rate of 2 °C min^{-1}. The sample collected after cooling was the active carbon/sulfur composite. The preparation of the sulfur cathode pieces was as follows. 80 wt% of the carbon/sulfur composite, 10 wt% of Super P and 10 wt% of the LA133 binder (5 wt% in water) were evenly mixed with deionized water and fully stirred in deionized water for 12 h, and the acquired slurry was uniformly coated onto the carbon-coated side of aluminum foil using the doctor blading method. As-fabricated cathode pieces were dried overnight in a vacuum oven at 60 °C and finally cut into cathode discs with a diameter of 12 mm and a specific sulfur loading of 1.2–1.3 mg cm^{-2}.

2.2.2 Preparation of the symmetrical electrodes. The carbon/sulfur composite was replaced with the active material (Co_3ZnC@NC), and the other procedures were the same as those above to produce the final Co_3ZnC@NC-based working electrodes and counter electrodes of the symmetrical cells.

2.3 Material characterization

X-ray diffraction (XRD, Rigaku Ultima IV) with Cu Kα radiation (λ = 0.154 nm) was used to analyze the crystal structure and composition of the composite. The microstructure of the samples was analyzed by applying a scanning electron microscope (SEM, ZEISS) and transmission electron microscope (TEM, FEI-Talos F200S). X-ray photoelectron spectroscopy (XPS, Thermo Scientific K-Alpha) was used to characterize the composition and valence states of the elements in the composites. The carbon content in the composite was analyzed by thermogravimetric analysis (TGA, Rigaku TG/DTA8122) under an air atmosphere. The Brunauer–Emmett–Teller (BET) method was used to assess the specific surface area and the pore size distribution of the sample through Micromeritics ASAP 2460. For the static adsorption test, a 10 mg sample (Super P or Co_3ZnC@NC) was added into 2 mL of Li_2S_6 solution (5 mmol L^{-1}, DoDo Chem, LS-243) and left for 24 h. The obtained supernatant after adsorption was diluted to measure the UV-vis absorption behavior on a UV-2600 spectrophotometer.

2.4 Battery assembly and electrochemical measurement

2.4.1 Assembly of Li–S batteries and symmetrical cells. Battery assembly was carried out in a glove box filled with argon gas to fabricate CR 2032 button cells. Typically, to assemble Li–S batteries, a high-purity lithium plate acted as the anode while the above-mentioned sulfur electrode acted as the cathode. The catalyst-modified separator or commercial separator (Celgard 2500) is assumed to be the separator. The electrolyte was composed of 1.0 M lithium bis(trifluoromethanesulphonyl) imide (LiTFSI) dissolving in mixed 1,2-dimethoxyethane (DME) and 1,3-dioxolane (DOL) solvent (DME : DOL = 1 : 1 vol%) by incorporating 1.0 wt% lithium nitrate ($LiNO_3$) as the additive. For the assembly of symmetrical cells, two identical Co_3ZnC@NC-based electrodes acted as the working electrode and the counter electrode, respectively. A commercial separator (PP, Celgard 2500) was used as the separator, and the electrolyte (20 μL) was composed of 0.2 mol L^{-1} Li_2S_6, 1.0 M LiTFSI and 1.0 wt% $LiNO_3$ in the mixed solvent of DME and DOL (v_{DME}/v_{DOL} = 1 : 1).

2.4.2 Electrochemical characterizations. Several electrochemical tests were performed on the CHI660E and NEWARE battery systems for the assembled coin cells. Charging–discharging tests were performed under constant current to determine the specific capacities, cyclic stability and rate performance. Cyclic voltammetry (CV) tests used an operating voltage range of 1.7–2.8 V and a scanning rate of 0.1–0.5 mV s^{-1}. The AC electrochemical impedance spectroscopy (EIS) responses were recorded over the frequency range of 0.01 Hz to 100 kHz. CV curves of the symmetric cells were obtained at a scanning rate of 5 mV s^{-1} and a voltage window of −1.0 to 1.0 V. For the lithium sulfide deposition/nucleation experiments, the coin cell was first discharged at a constant current of 0.112 mA to 2.12 V and then kept at a constant potential of 2.05 V until the current was below 0.01 mA to ensure that Li_2S was completely nucleated. For the Li_2S dissolution experiment, the battery was first discharged to 1.80 V at a constant current of 0.01 mA and then charged at a constant potential of 2.40 V until the current was down to 0.01 mA such that Li_2S was completely dissolved to obtain the current–time curve.

3. Results and discussion

The schematic of the synthesis of the bimetal carbide-embedded composite is shown in Fig. 1a. Particularly, Co_3ZnC@NC was derived from the formation and post-pyrolysis of the PBA precursor. Following a simple one-pot process, $Co(CN)_6^{3-}$ reactants were spontaneously coordinated with Co^{2+} and Zn^{2+} for co-precipitation in the dispersion according to a suitable stoichiometric ratio. After sufficient aging and separation/purification, the cobalt–zinc PBA precursor was received, as evident by the series of characteristic diffraction peaks belonging to $Zn_3[Co(CN)_6]_2 \cdot (H_2O)_{12}$ (PDF #89-3739) (Fig. 1b). Finally, the PBA precursor turned to carbon-wrapped metal compounds after high-temperature calcination under an inert atmosphere, forming the Co_3ZnC@NC composite. As demonstrated by the XRD pattern in Fig. 1b, there is a convex peak near 2θ of 26.5°, which results from the characteristic graphitic plane of the nitrogen-doped carbon component in the composite. Moreover, the set of characteristic peaks centered at 2θ of 34.0°, 41.9°, 48.8° and 71.5° corresponds to the (110), (111), (200) and (220) planes of the Co_3ZnC phase (PDF #29-0524).[31] In addition, the composition of the composite was further distinguished by thermogravimetric analysis (TGA) conducted in an air atmosphere. Fig. 1c shows the thermogravimetric curve of Co_3ZnC@NC. This demonstrates two obvious steps for mass loss upon calcination. The first weight decline occurs in the range of 300–400 °C, which accounts for a loss portion of 28.6% and can be attributed to the oxidation decomposition of the nitrogen-doped carbon species in the outer layer of the composite. The second weight loss appears in the range of 550–650 °C largely caused by the oxidation of the

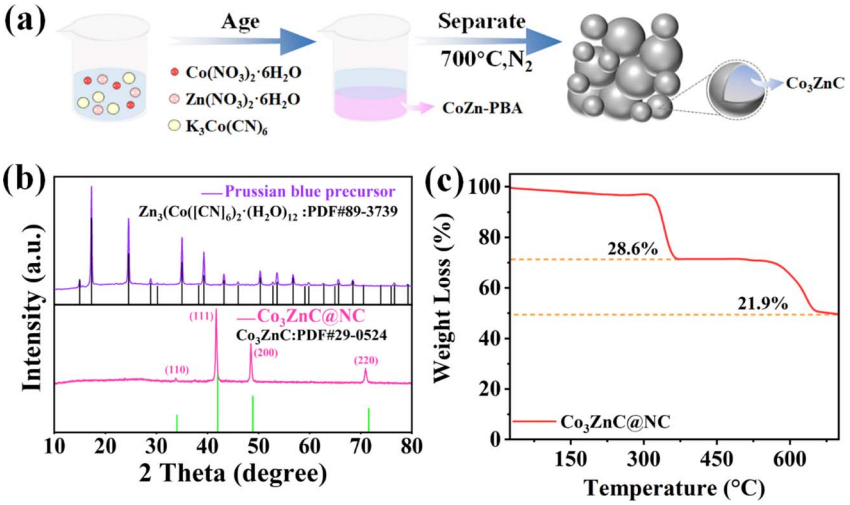

Fig. 1 (a) Schematic preparation of the Co_3ZnC@NC composite, (b) XRD patterns of different samples, and (c) thermogravimetric curve of Co_3ZnC@NC.

inner carbonaceous species and metal carbides component, leading to a loss rate of 21.9%. The results indicate that there are considerable amounts of carbon components in the Co_3ZnC@NC composite.

SEM images of the as-synthesized composite are shown in Fig. 2a and b. It can be observed that Co_3ZnC@NC is basically composed of relatively dispersed and uniform nanoparticles. Some of these densely packed nanoparticles are connected by a few short carbon nanotubes (Fig. 2c), which is not uncommon because the presence of active cobalt-based species can often catalyze the growth of carbon nanotubes under high-temperature carbonization.[36] The fine structure of Co_3ZnC@NC is illustrated in Fig. 2d, revealing that Co_3ZnC@NC mainly comprises irregular nanoparticles with particle sizes of 30–50 nm. According to Fig. 2e and f, Co_3ZnC@NC demonstrates a typical core–shell nanostructure, where the internal Co_3ZnC nanocrystals are stably surrounded by thin N-doped carbon shells. Moreover, the lattice spacing of the inner nanoparticles is about 0.217 nm and

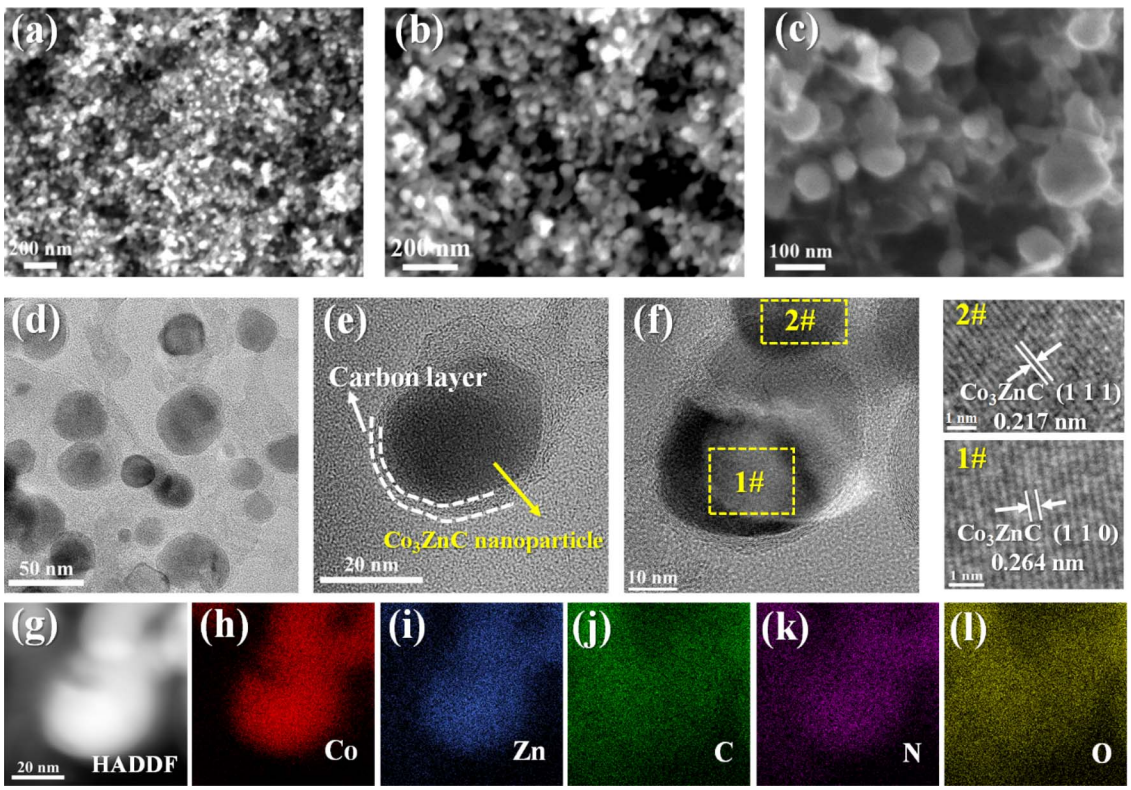

Fig. 2 SEM (a–c), HR-TEM (d–f), and EDS mapping (g–l) images of Co_3ZnC@NC.

0.264 nm, corresponding to the characteristic (110) and (111) faces of the Co_3ZnC nanocrystals. Fig. 2g–l displays the energy disperse spectroscopy (EDS) mapping images of Co_3ZnC@NC, showing that Co, Zn, C, N, and O elements are homogeneously distributed in the core/shell structured nanoparticles. Obviously, Co and Zn species are dominantly concentrated in the core of the nanoparticle, while C and N elements exhibit aggregated distribution in the outer layer of the nanoparticle along with apparent spreading over the entire nanoparticle. Unavoidably, the uniform distribution of O element in the composite is reasonable because many active nanocarbon or metal nanoparticles often endure slight oxidation to introduce oxygen-containing groups on the surfaces upon synthesis and utilization.[37] All the above results confirm the effective hybridization of Co_3ZnC nanocrystals and N-doped carbon to form core–shell structured Co_3ZnC@NC.

Fig. 3a demonstrates the N_2 adsorption/desorption isotherms of Co_3ZnC@NC. The BET surface area of Co_3ZnC@NC is determined to be 53.40 $m^2\ g^{-1}$. Thus, the pore volume of the Co_3ZnC@NC composite is 0.202 $cm^3\ g^{-1}$ with an average pore size of 16.26 nm. The pore size distribution reveals that Co_3ZnC@NC is characterized by a hierarchical structure consisting of considerable micropores and sufficient mesopores. These hierarchical pores can ensure the appropriate penetration of the electrolyte into the catalyst to improve ion diffusion. Moreover, more exposed active sites are available to positively anchor/adsorb the soluble LiPSs to accelerate the catalytic conversion rate of LiPSs[38] to confine the LiPSs at the cathode reaction interfaces with reduced shuttling effect.

To investigate the surface chemical composition and electronic state of the Co_3ZnC@NC catalyst materials, X-ray photoelectron spectroscopy (XPS) characterization was performed. The full spectrum further verified the coexistence of the main characteristic peaks of C 1s, N 1s, O 1s, Co 2p, and Zn 2p. The contents of C, N, O, Co, and Zn elements on the surface of Co_3ZnC@NC were 74.32%, 12.69%, 8.31%, 1.35% and 3.33%, respectively. Fig. 3b shows the high-resolution Co 2p spectrum of Co_3ZnC@NC. The pair of sharp peaks at 778.1 and 793.1 eV can be ascribed to the characteristic Co^0 species, suggesting the adequate proportion of metallic Co present in the bimetal carbides under pyrolysis. This result agrees well with the above-mentioned observation that minor carbon nanotubes were generated by Co-catalyzed growth during the carbonization synthesis of Co_3ZnC@NC.[39] The prominent peaks at 778.8 and 793.7 eV correspond to the Co^{2+} species, along with two satellite peaks occurring at 781.9 and 796.8 eV. It is rational that the coexistence of Co^0 and Co^{2+} could effectively balance the valence states of Co active sites, which is beneficial for enhancing the chemical adsorption and targeted anchoring of LiPSs by the active electrocatalyst during battery reactions.[35] In the high-resolution Zn 2p spectrum (Fig. 3c), two featured peaks at 1021.8 and 1044.9 eV can be assigned to Zn^{2+}. Previous findings have illustrated that the presence of a second metal species (*e.g.* Zn^{2+}) can cooperate with Co^{2+} to act as a reservoir, achieving synergistic adsorption and catalytic conversion of LiPSs.[40,41] For the C 1s spectrum illustrated in Fig. 3d, the diffraction peaks are C–C (284.8 eV), C–N (285.7 eV) and C=O (288.3 eV), indicating that the carbon layer on the surface of Co_3ZnC@NC is rich in abundant C–N bonding. Such electronegative nitrogen-rich carbon coating can introduce more disordered defects, increase the surface chemical affinity of the Co_3ZnC@NC composite toward LiPSs, and stabilize the internal bimetal carbides nanocrystals upon electrochemical cycling.

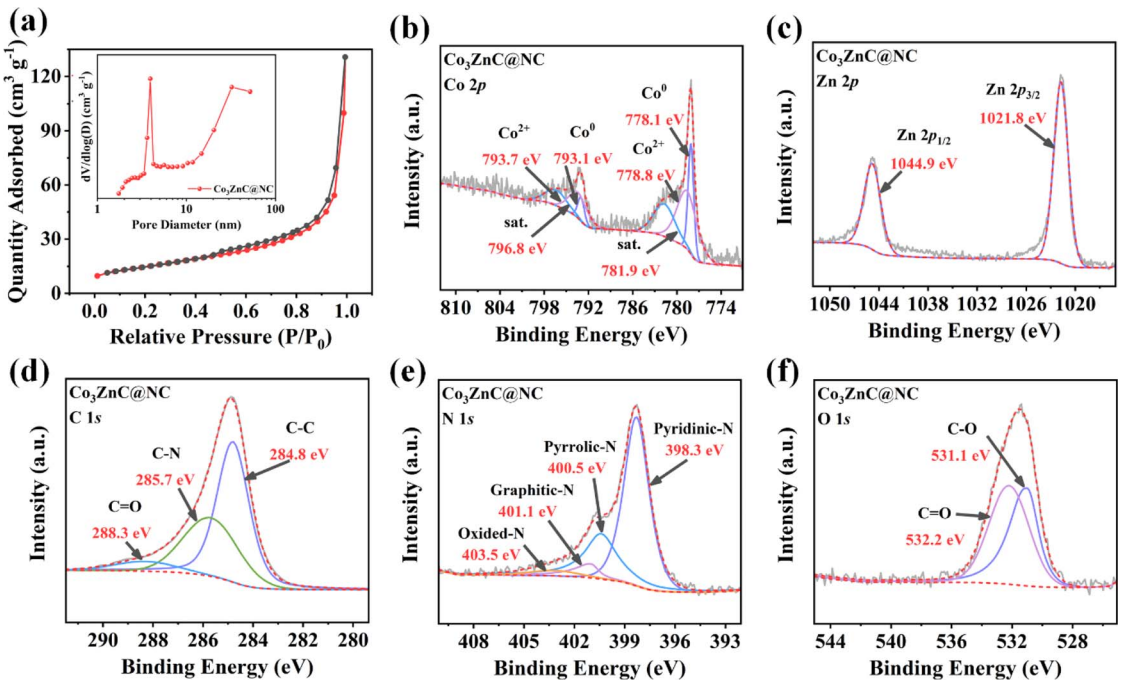

Fig. 3 (a) Nitrogen adsorption/desorption curves and pore size distribution (inset) of Co_3ZnC@NC; Co 2p (b), Zn 2p (c), C 1s (d), N 1s (e) and O 1s (f) spectrum of Co_3ZnC@NC.

According to Fig. 3e of the N 1s spectrum, the peak corresponds to pyridinic N (398.3 eV), pyrrolic N (400.5 eV), graphitic N (401.1 eV) and N oxides (403.5 eV). Conformably, the apparently high content of pyridinic N and pyrrolic N promoted electron transfer on the surface of the hybrid electrocatalyst, favoring the redox reactions of long-chain LiPSs.[42] For the O 1s spectrum (Fig. 3e), the C–O bond at 531.1 eV and the C=O bond at 532.2 eV further infer the partial oxidation on the surface of Co_3ZnC@NC.

Fig. 4a shows the UV-vis absorption curves and corresponding optical photos of different samples after the static adsorption of Li_2S_6. Compared to Super P and the blank samples, Co_3ZnC@NC exhibited obviously increased adsorption capacity and high trapping ability toward polysulfides, which can be verified by the cleared color and the almost disappeared characteristic peaks of the Li_2S_6 solution in the UV-vis absorption spectrum.[25] To verify the electrocatalytic performance of Co_3ZnC@NC for LiPSs, cyclic voltammetry (CV) tests of symmetric cells were performed with Li_2S_6 solution as the electrolyte across the operating voltage range of −1.0 V to 1.0 V. In addition, a control cell using an electrolyte without Li_2S_6 was investigated as the reference. As shown in Fig. 4b, the reference cell basically produces a negligible current contribution, while the symmetric cell containing Li_2S_6 exhibits obvious current response and significant redox peaks at −0.06 V and 0.06 V, indicating the adorable electrochemical properties of the Co_3ZnC@NC composite for catalyzing the redox conversion of soluble LiPSs.

To further examine the electrochemical performance of the designed catalyst in actual batteries, Co_3ZnC@NC was used as an interlayer catalyst to modify the commercial PP separator, obtaining the Co_3ZnC@NC/PP-based Li–S battery. Unless otherwise mentioned, all the assembled Li–S batteries adopted a cathode with a sulfur loading of 72 wt% (Fig. S1†). Fig. 4c shows the Nyquist plots of fresh batteries based on Co_3ZnC@NC/PP and PP separator through electrochemical impedance spectroscopy (EIS) characterization. It is reasonable that the entire internal resistance of the battery significantly decreases after the involvement of Co_3ZnC@NC. Thus, the charge transfer resistance (R_{ct}) of the Co_3ZnC@NC/PP battery (24.2 Ω) is much smaller than that of the PP battery (47.5 Ω), suggesting that the Co_3ZnC@NC interlayer catalyst can

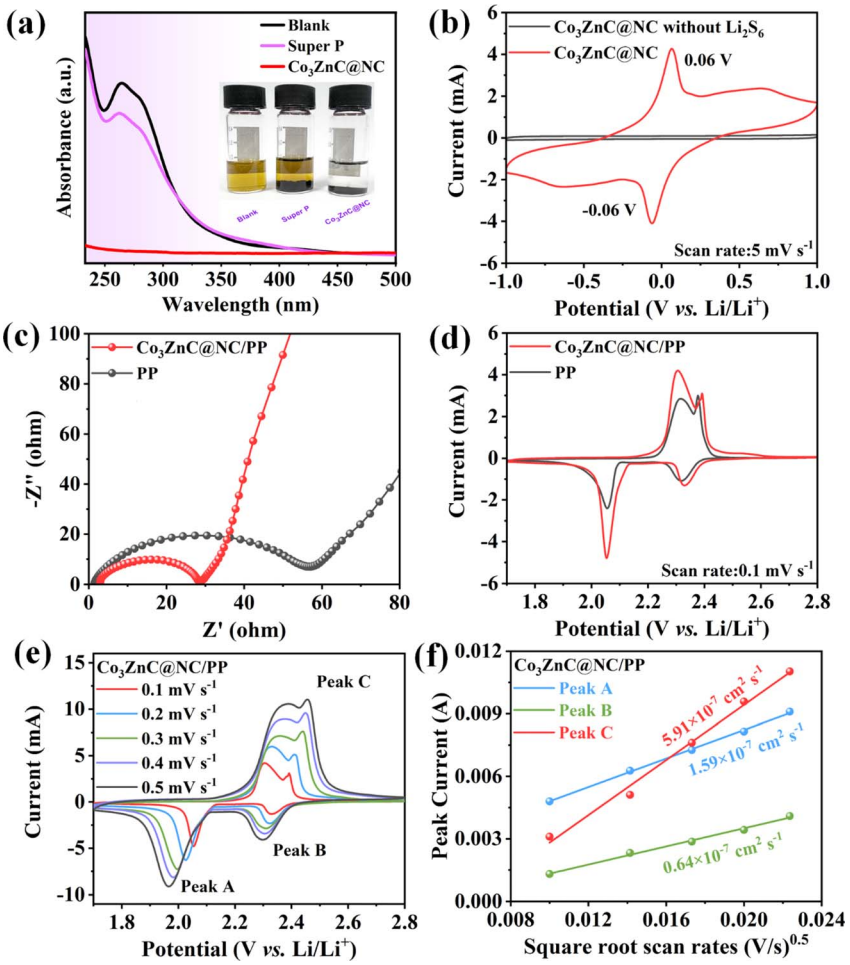

Fig. 4 (a) UV-vis absorption curves of different samples after Li_2S_6 adsorption and correlated photos of the static adsorption experiment of Li_2S_6 solution (inset); (b) CV curves of Co_3ZnC@NC-based symmetrical cells at a scan rate of 5 mV s^{-1}; (c) EIS curves of fresh Co_3ZnC@NC/PP and the PP batteries before cycling; (d) CV curves of Co_3ZnC@NC/PP and PP-based Li–S batteries at a scanning rate of 0.1 mV s^{-1}; (e) CV curves of the Co_3ZnC@NC/PP battery at different scanning rates; and (f) linear fitting plots of the three peak currents for the Co_3ZnC@NC/PP battery.

dramatically improve the interfacial charge-transfer by simultaneously providing sufficient electrocatalytic sites and a good conductive network, leading to accelerated redox kinetics of sulfur species, especially on the cathode side of the battery.[43,44] Moreover, the redox reaction process of Li–S batteries was investigated in the operating voltage range (1.7–2.8 V) using CV at a low sweep rate of 0.1 mV s^{-1}. As shown in Fig. 4d, two separate reduction peaks centered at 2.34 and 2.05 V appear in the cathodic sweeping process, while two distinct peaks (2.3–2.5 V) in the anodic sweeping process can be observed. The former results from the stepwise production of long-chain Li_2Sn ($4 \leq n < 8$) and short-chain polysulfides ($1 \leq n < 4$) by reducing the elemental sulfur.[45] The latter corresponds to the backward oxidation of lithium sulfide to Li_2Sn ($2 \leq n \leq 8$). With the incorporation of Co_3ZnC@NC, the relevant battery delivers much stronger peak currents and reduced polarization potentials. It can be concluded that Co_3ZnC@NC exhibits a superior catalytic ability to facilitate reaction kinetics and improve the redox conversion of LiPSs during the battery charge/discharge process. Moreover, CV tests were performed on the PP battery and Co_3ZnC@NC/PP battery under different scanning rates. As demonstrated in Fig. 4e, the peak current and electrode polarization of the Li–S battery gradually increase as the scanning rate increases. Using the Randles–Sevcik equation, we analyzed the relationship between the peak current (I_p) of the characteristic redox peaks and the square root of the scanning rate ($v^{0.5}$).[46] As displayed in Fig. 4f, there is a certain linear relationship between I_p and $v^{0.5}$. In particular, the lithium ion diffusion coefficients (D_{Li^+}) of peaks A, B and C are calculated to be 1.59×10^{-7}, 0.64×10^{-7} and 5.91×10^{-7} cm^2 s^{-1}, respectively, which are obviously higher than those of the PP battery (Fig. S2 and S3†), further confirming the favorable ion transport and electrochemical reversibility by the Co_3ZnC@NC catalyst. Notably, the D_{Li^+} of the oxidation peak is significantly higher than the others. This infers that Co_3ZnC@NC could behave better at the catalytic conversion of short-chain Li_2Sn to long-chain LiPSs rather than the opposite reduction pathway.[47]

Fig. 5a shows the cycling performances of Li–S batteries based on Co_3ZnC@NC/PP, Super P/PP and PP separator under a current density of 0.5C. Compared to the other two counterparts, the Co_3ZnC@NC/PP exhibits extremely improved discharge capacities and cycling stability. In particular, the initial discharge specific capacity of the Co_3ZnC@NC/PP battery is 1144.6 mA h g^{-1} higher than that of Super P/PP (1003.6 mA h g^{-1}) and PP battery (635.1 mA h g^{-1}). After 100 continuous charge/discharge cycles, the Co_3ZnC@NC/PP battery can maintain a high discharge capacity of 962.6 mA h g^{-1}, yielding a retention rate of 84.1%, which is superior to that of the Super P/PP (79.6%) and PP battery (61.6%) with much lower retention capacity. Moreover, the high coulombic efficiencies of the Co_3ZnC@NC/PP battery during cycling demonstrate its excellent reversibility and durability during charge/discharge reactions.[48,49] Correspondingly, the initial galvanostatic charge–discharge curves of batteries with different separators are compared, as depicted in Fig. 5b, which magnifies the relatively low electrode polarization of the Co_3ZnC@NC/PP battery. Further, after 100 successive cycles, the electrode polarization of the Co_3ZnC@NC/PP battery did not

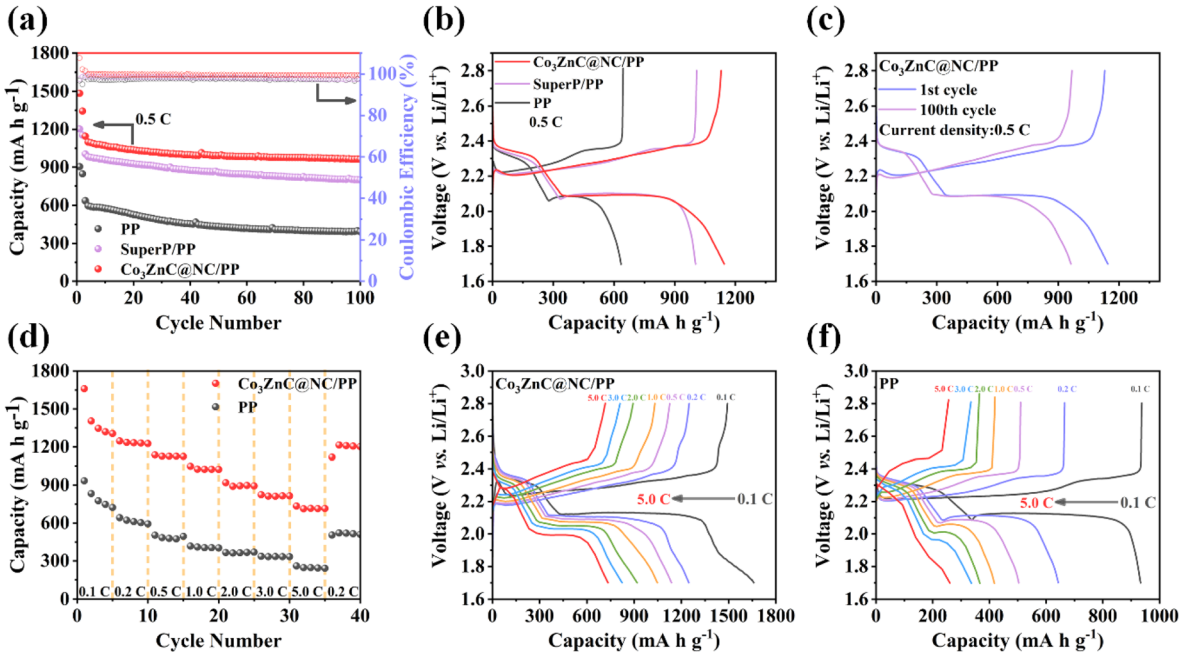

Fig. 5 (a) Cycling capacities and coulombic efficiencies of Li–S batteries with Co_3ZnC@NC/PP, Super P/PP and PP separator at 0.5C. The batteries were measured at 0.1C for the initial two cycles. (b) Comparison of the initial charge/discharge voltage–capacity curves of different batteries at 0.5C; (c) comparison of the first and 100th galvanostatic charge–discharge curves of Co_3ZnC@NC/PP-based Li–S battery at 0.5C; (d) rate performances of Li–S batteries with different separators; and (e and f) galvanostatic charge and discharge curves of Li–S batteries with different separators under different current densities.

change much (Fig. 5c). This suggests that the Co_3ZnC/NC interlayer catalyst can effectively improve the electrochemical reversibility and capacity performance of Li–S batteries. According to the S 2p spectrum of Co_3ZnC@NC after cycling at 0.5C for 50 cycles (Fig. S4a†), the prominent Co–S bonding further infers the strong chemical affinity and anchoring ability of Co_3ZnC@NC toward polysulfides. Moreover, the evident negative shift of the N 1s peaks along with the positive shifts of both Co 2p peaks and Zn 2p peaks indicates the redistributed electron density of the metal centers or the metal–N moieties (Fig. S4b–d†), which could act as active sites for enhanced polysulfide interaction and catalytic conversion.

The rate performance of the Li–S batteries is demonstrated in Fig. 5d. Co_3ZnC@NC/PP-based battery delivers a specific discharge capacity of 1659.8 mA h g^{-1} at 0.1C. As the current density incrementally increases to 0.2C, 0.5C, 1.0C, 2.0C, 3.0C and 5.0C, the corresponding specific capacity is 1246.9, 1136.7, 1047.3, 918.4, 823.4 and 734.0 mA h g^{-1}, greatly surpassing that of the PP battery. Then, when the current density returns to 0.2C, the discharge specific capacity can still be restored to 1201.7 mA h g^{-1} for the Co_3ZnC@NC/PP battery. This indicates that the active sites of the Co_3ZnC@NC composite can achieve stable adsorption and electrocatalytic promotion of LiPSs upon lithium storage at different current densities, thus contributing to the high specific capacities and excellent rate capability of the battery at high rates. Based on the charge–discharge curves illustrated in Fig. 5e and f, the increases in the voltage gap of the Co_3ZnC@NC/PP battery are significantly smaller than those of the PP battery at different current densities, further proving the efficient utilization of active sulfur and superb cycling stability by involving the Co_3ZnC@NC interlayer as a polysulfide mediator in Li–S batteries during battery operation.

Furthermore, the long-term cyclic stability of the designed Li–S batteries was investigated. As presented in Fig. 6a, the Co_3ZnC@NC/PP-based battery delivers an initial discharge capacity of 996.6 mA h g^{-1} at 1.0C. After 250 charge/discharge cycles, the battery can well maintain a reversible specific capacity of 695.8 mA h g^{-1}, exhibiting capacity retention of 69.8% and an average decay rate per cycle of about 0.121%. Additionally, the coulombic efficiencies of the battery are stably above 96%. The results demonstrate the distinctly enhanced battery stability and excellent cycling performance by the

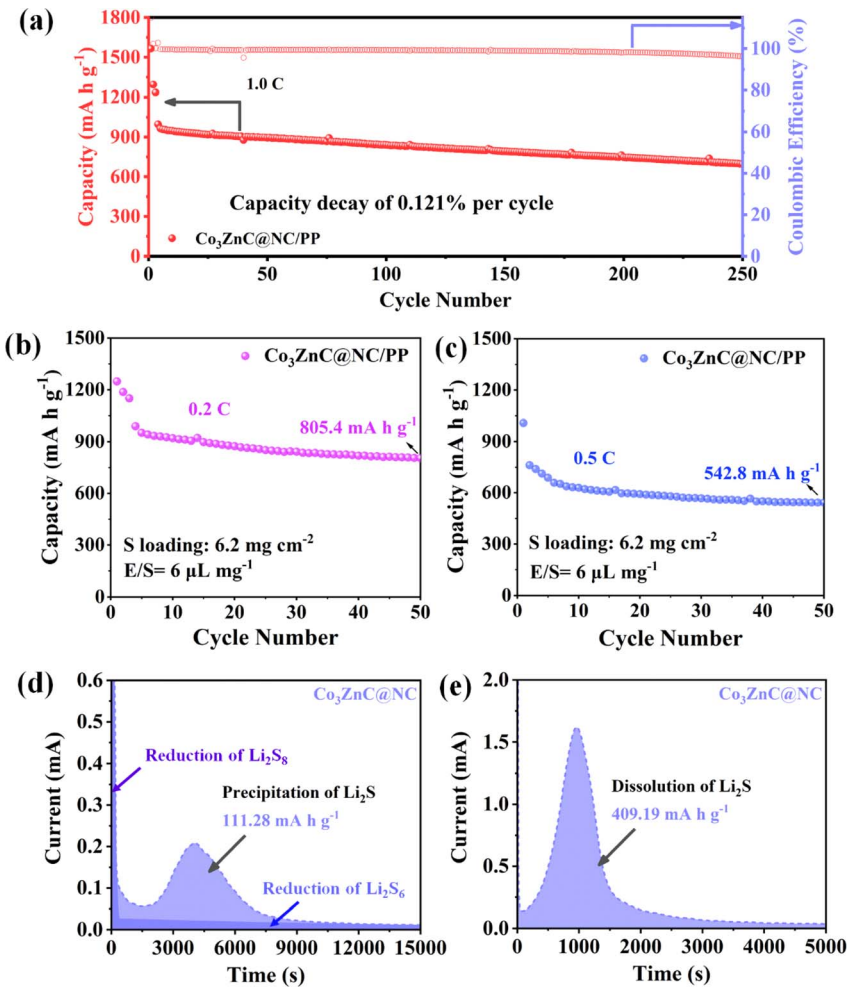

Fig. 6 (a) Long-cycle capacities and coulombic efficiencies of the Co_3ZnC@NC/PP battery at 1.0C. The battery was measured at 0.1C for the initial two cycles. Cycling performance of the Co_3ZnC@NC/PP battery with high sulfur loading at 0.2C (b) and 0.5C (c). (d) Potentiostatic discharge current–time plot of Co_3ZnC@NC. (e) Potentiostatic charging current–time plot of Co_3ZnC@NC.

Co_3ZnC@NC-modified functional separator upon long cycling. When the sulfur loading of the cathode was drastically elevated to 6.2 mg cm^{-2} (*i.e.* E/S of 6 μL mg^{-1}), the corresponding Co_3ZnC@NC/PP battery can maintain a high discharge capacity of 805.4 mA h g^{-1} (areal capacity of ~5 mA h cm^{-2}) at 0.2C (Fig. 6b) and 542.8 mA h g^{-1} at 0.5C (Fig. 6c) even after 50 continuous cycles, shedding light on its superior cycling stability and promising practical potential toward high-specific energy output with lean electrolyte (Table S1†).

To further elucidate the positive role and key electrocatalytic performance of the Co_3ZnC@NC/PP catalyst for the redox conversion of LiPSs, typical nucleation/dissolution experiments were performed by assembling the coin battery with the Co_3ZnC@NC electrode and the Li_2S_8-contained electrolyte.[50,51] Fig. 6d illustrates the potentiostatic discharge current–time plot of Co_3ZnC@NC at an operating voltage of 2.05 V. The specific capacity of the Co_3ZnC@NC electrode toward Li_2S nucleation is calculated to be 111.28 mA h g^{-1}. Furthermore, by fitting the charging current–time plot of the Co_3ZnC@NC electrode operating at 2.40 V, a high specific capacity of 409.19 mA h g^{-1} is achieved for Co_3ZnC@NC toward Li_2S dissolution (Fig. 6e). The relatively adorable nucleation/dissolution ability of Li_2S strongly confirms the chemical affinity and superior catalytic activity of the functional Co_3ZnC@NC layer. Co_3ZnC@NC could dominantly inhibit polysulfide shuttling by facilitating the interfacial charge transfer process and reducing the activation barrier for the phase nucleation of polysulfides[52,53] to achieve accelerated redox kinetics of LiPSs and improved sulfur utilization of correlated Li–S batteries.

4. Conclusion

In summary, a hybrid electrocatalyst of Co_3ZnC-embedded nanospheres was developed as an efficient separator interlayer for rechargeable Li–S batteries. Using one-pot synthesis combined carbonization of Prussian blue analogue precursor, core–shell-structured Co_3ZnC@NC composite was obtained, showing advantages of high conductivity, hierarchical porosity, excellent adsorption properties and rich active sites toward LiPSs. Results demonstrated that Co_3ZnC@NC could act as a suitable polysulfide mediator by effectively lowering the interfacial charge-transfer resistance and improving the catalytic reversibility, thus contributing to enhanced redox kinetics of LiPSs upon battery reactions. Consequently, Co_3ZnC@NC/PP-based Li–S batteries achieved superior rate capabilities (734.0 mA h g^{-1} at 5.0C), excellent cyclic durability (capacity retention rate of 84.1% after 100 cycles at 0.5C) and significant sulfur utilization efficiency even under a high sulfur loading of 6.2 mg cm^{-2}. This study illustrates a simple and cost-effective strategy for constructing advanced bimetal compound/carbon-based hybrid catalysts for high-performance renewable energy devices.

Data availability

The raw/processed data used in this study cannot be shared at this time, as the data also form part of an ongoing study.

Conflicts of interest

The authors declare no conflict of interest.

Acknowledgements

This work was supported by the science and technology project of China Southern Power Grid (grant number YNKJXM20222118, YNKJXM20222131, YNKJXM20222043).

References

1 A. Manthiram, Y. Fu, S.-H. Chung, C. Zu and Y.-S. Su, Rechargeable lithium-sulfur batteries, *Chem. Rev.*, 2014, **114**, 11751–11787.
2 A. Manthiram, S.-H. Chung and C. Zu, Lithium-sulfur batteries: progress and prospects, *Adv. Mater.*, 2015, **27**, 1980–2006.
3 Z. W. Seh, Y. Sun, Q. Zhang and Y. Cui, Designing high-energy lithium-sulfur batteries, *Chem. Soc. Rev.*, 2016, **45**, 5605–5634.
4 Y. Hu, W. Chen, T. Lei, Y. Jiao, J. Huang, A. Hu, C. Gong, C. Yan, X. Wang and J. Xiong, Strategies toward high-loading lithium-sulfur battery, *Adv. Energy Mater.*, 2020, **10**, 2000082.
5 J. Li, Z. Niu, C. Guo, M. Li and W. Bao, Catalyzing the polysulfide conversion for promoting lithium sulfur battery performances: a review, *J. Energy Chem.*, 2021, **54**, 434–451.
6 Z. Du, X. Chen, W. Hu, C. Chuang, S. Xie, A. Hu, W. Yan, X. Kong, X. Wu, H. Ji and L.-J. Wan, Cobalt in nitrogen-doped graphene as single-atom catalyst for high-sulfur content lithium-sulfur batteries, *J. Am. Chem. Soc.*, 2019, **141**, 3977–3985.
7 Y. Liu, Z. Ma, G. Yang, Z. Wu, Y. Li, J. Gu, J. Gautam, X. Gong, A. N. Chishti, S. Duan, C. Chen, M. Chen, L. Ni and G. Diao, Multifunctional $ZnCo_2O_4$ quantum dots encapsulated in carbon carrier for anchoring/catalyzing polysulfides and self-repairing lithium metal anode in lithium-sulfur batteries, *Adv. Funct. Mater.*, 2022, **32**, 2109462.
8 T. Huang, Y. Sun, J. Wu, J. Jin, C. Wei, Z. Shi, M. Wang, J. Cai, X.-T. An, P. Wang, C. Su, Y.-y. Li and J. Sun, A dual-functional fibrous skeleton implanted with single-atomic Co-Nx dispersions for longevous Li-S full batteries, *ACS Nano*, 2021, **15**, 14105–14115.
9 X. Yang, X. Gao, Q. Sun, S. P. Jand, Y. Yu, Y. Zhao, X. Li, K. Adair, L.-Y. Kuo, J. Rohrer, J. Liang, X. Lin, M. N. Banis, Y. Hu, H. Zhang, X. Li, R. Li, H. Zhang, P. Kaghazchi, T.-K. Sham and X. Sun, Promoting the transformation of Li2S2 to Li2S: significantly increasing utilization of active materials for high-sulfur-loading Li-S batteries, *Adv. Mater.*, 2019, **31**, 1901220.
10 X. Sun, Y. Qiu, B. Jiang, Z. Chen, C. Zhao, H. Zhou, L. Yang, L. Fan, Y. Zhang and N. Zhang, Isolated Fe-Co heteronuclear diatomic sites as efficient bifunctional catalysts for high-performance lithium-sulfur batteries, *Nat. Commun.*, 2023, **14**, 291.

11 K. Zhang, Z. Chen, R. Ning, S. Xi, W. Tang, Y. Du, C. Liu, Z. Ren, X. Chi, M. Bai, C. Shen, X. Li, X. Wang, X. Zhao, K. Leng, S. J. Pennycook, H. Li, H. Xu, K. P. Loh and K. Xie, Single-atom coated separator for robust lithium-sulfur batteries, *ACS Appl. Mater. Interfaces*, 2019, **11**, 25147–25154.

12 B. Wei, C. Shang, X. Wang and G. Zhou, Conductive FeOOH as multifunctional interlayer for superior lithium-sulfur batteries, *Small*, 2020, **16**, 2002789.

13 S. Wang, X. Liu, H. Duan, Y. Deng and G. Chen, Fe3C/Fe nanoparticles embedded in N-doped porous carbon nanosheets and graphene: a thin functional interlayer for PP separator to boost performance of Li-S batteries, *Chem. Eng. J.*, 2021, **415**, 129001.

14 Y. Peng, Y. Zhang, Y. Wang, X. Shen, F. Wang, H. Li, B.-J. Hwang and J. Zhao, Directly coating a multifunctional interlayer on the cathode via electrospinning for advanced lithium-sulfur batteries, *ACS Appl. Mater. Interfaces*, 2017, **9**, 29804–29811.

15 Q. Li, Y. Liu, L. Yang, Y. Wang, Y. Liu, Y. Chen, X. Guo, Z. Wu and B. Zhong, N, O co-doped chlorella-based biomass carbon modified separator for lithium-sulfur battery with high capacity and long cycle performance, *J. Colloid Interface Sci.*, 2021, **585**, 43–50.

16 M.-e. Zhong, J. Guan, J. Sun, H. Guo, Z. Xiao, N. Zhou, Q. Gui and D. Gong, Carbon nanodot-decorated alveolate N, O, S tridoped hierarchical porous carbon as efficient electrocatalysis of polysulfide conversion for lithium-sulfur batteries, *Electrochim. Acta*, 2019, **299**, 600–609.

17 F. Ma, B. Yu, X. Zhang, Z. Zhang, K. Srinivas, X. Wang, D. Liu, B. Wang, W. Zhang, Q. Wu and Y. Chen, WN0.67-embedded N-doped graphene-nanosheet interlayer as efficient polysulfide catalyst and absorbant for high-performance lithium-sulfur batteries, *Chem. Eng. J.*, 2022, **431**, 133439.

18 C. Zhang, C. Ma, W. Zhang, Y. Wang, Z. U. Rehman, X. Shen and S. Yao, CoFe2O4 nanoparticles modified amidation of N-doped carbon nanofibers hybrid catalysts to accelerate electrochemical kinetics of Li-S batteries with high sulfur loading, *Chem. Eng. J.*, 2024, **481**, 148374.

19 H. Lin, S. Zhang, T. Zhang, S. Cao, H. Ye, Q. Yao, G. W. Zheng and J. Y. Lee, A cathode-integrated sulfur-deficient Co9S8 catalytic interlayer for the reutilization of "lost" polysulfides in lithium-sulfur batteries, *ACS Nano*, 2019, **13**, 7073–7082.

20 W. Yao, J. Xu, L. Ma, X. Lu, D. Luo, J. Qian, L. Zhan, I. Manke, C. Yang, P. Adelhelm and R. Chen, Recent progress for concurrent realization of shuttle-inhibition and dendrite-free lithium-sulfur batteries, *Adv. Mater.*, 2023, **35**, 2212116.

21 Q. Liang, S. Wang, Y. Yao, P. Dong and H. Song, Transition metal compounds family for Li-S batteries: the DFT-guide for suppressing polysulfides shuttle, *Adv. Funct. Mater.*, 2023, **33**, 2300825.

22 K. Wang, H. Yang, R. Yan, C. Chen, C. Wu, W. Chen, Z. He, G. Huang and L. Chang, Ni-CoSe2 heterojunction coated by N-doped carbon for modified separators of high-performance Li-sulfur batteries, *RSC Adv.*, 2024, **14**, 15358–15364.

23 L. B. Liang, L. T. Gao, Z. Y. Ma, Q. Cao, B. Jing, X. Y. Wang, Y. Lu and W. X. Wang, Phosphorus-doped few-layer graphite wrapped metallic cobalt as interlayer for advanced lithium–sulfur batteries, *Mater. Today Energy*, 2023, **37**, 101415.

24 L. Wang, W. Hua, X. Wan, Z. Feng, Z. Hu, H. Li, J. Niu, L. Wang, A. Wang, J. Liu, X. Lang, G. Wang, W. Li, Q.-H. Yang and W. Wang, Design rules of a sulfur redox electrocatalyst for lithium-sulfur batteries, *Adv. Mater.*, 2022, **34**, 2110279.

25 M. Wang, X. Zhou, X. Cai, H. Wang, Y. Fang and X. Zhong, Hierarchically porous, ultrathin N-doped carbon nanosheets embedded with highly dispersed cobalt nanoparticles as efficient sulfur host for stable lithium-sulfur batteries, *J. Energy Chem.*, 2020, **50**, 106–114.

26 J. L. Cheong, C. Hu, W. Liu, M.-F. Ng, M. B. Sullivan and J. Y. Ying, 3D carbonaceous nanostructured transition metal nitride, carbonitride and carbide as polysulfide regulators for lithium-sulfur batteries, *Nano Energy*, 2022, **102**, 107659.

27 Y. Wang, J. Shen, L.-C. Xu, Z. Yang, R. Li, R. Liu and X. Li, Sulfur-functionalized vanadium carbide MXene (V2CS2) as a promising anchoring material for lithium-sulfur batteries, *Phys. Chem. Chem. Phys.*, 2019, **21**, 18559–18568.

28 F. Zhou, Z. Li, X. Luo, T. Wu, B. Jiang, L.-L. Lu, H.-B. Yao, M. Antonietti and S.-H. Yu, Low cost metal carbide nanocrystals as binding and electrocatalytic sites for high performance Li-S batteries, *Nano Lett.*, 2018, **18**, 1035–1043.

29 T. Zhou, J. Liang, S. Ye, Q. Zhang and J. Liu, Fundamental, application and opportunities of single atom catalysts for Li-S batteries, *Energy Storage Mater.*, 2023, **55**, 322–355.

30 S. Gu, S. Xu, X. Song, H. Li, Y. Wang, G. Zhou, N. Wang and H. Chang, Electrostatic potential-induced Co-N4 active centers in a 2D conductive metal-organic framework for high-performance lithium-sulfur batteries, *ACS Appl. Mater. Interfaces*, 2022, **14**, 50815–50826.

31 M. Wang, G. Ruan, Q. Gao, S. Zhang, H. Wang, S. Yang, Y. Fang and X. Cai, Zn2+-modulated bimetallic carbides synergized with macro-mesoporous N-rich carbon enabling accelerated polysulfides conversion for high-performance Li-S batteries, *Chem. Eng. J.*, 2022, **431**, 133205.

32 W. Bao, D. Su, W. Zhang, X. Guo and G. Wang, 3D metal carbide@mesoporous carbon hybrid architecture as a new polysulfide reservoir for lithium-sulfur batteries, *Adv. Funct. Mater.*, 2016, **26**, 8746–8756.

33 Z. Zhang, J.-N. Wang, A. H. Shao, D.-G. Xiong, J.-W. Liu, C.-Y. Lao, K. Xi, S.-Y. Lu, Q. Jiang, J. Yu, H.-L. Li, Z.-Y. Yang and R. V. Kumar, Recyclable cobalt-molybdenum bimetallic carbide modified separator boosts the polysulfide adsorption-catalysis of lithium sulfur battery, *Sci. China Mater.*, 2020, **63**, 2443–2455.

34 X.-J. Hong, C.-L. Song, Z.-M. Wu, Z.-H. Li, Y.-P. Cai, C.-X. Wang and H. Wang, Sulfophilic and lithophilic sites in bimetal nickel-zinc carbide with fast conversion of polysulfides for high-rate Li-S battery, *Chem. Eng. J.*, 2021, **404**, 126566.

35 T. Yang, K. Liu, T. Wu, J. Zhang, X. Zheng, C. Wang and M. Chen, Rational valence modulation of bimetallic

carbide assisted by defect engineering to enhance polysulfide conversion for lithium-sulfur batteries, *J. Mater. Chem. A*, 2020, **8**, 18032–18042.

36 R. Wang, R. Wu, X. Yan, D. Liu, P. Guo, W. Li and H. Pan, Implanting single Zn atoms coupled with metallic Co nanoparticles into porous carbon nanosheets grafted with carbon nanotubes for high-performance lithium-sulfur batteries, *Adv. Funct. Mater.*, 2022, **32**, 2200424.

37 Y. Luo, D. Zhang, Y. He, W. Zhang, S. Liu, K. Zhu, L. Huang, Y. Yang, G. Wang, R. Yu, H. Shu, X. Wang and M. Chen, Intergrated morphology engineering and alloying strategy for FeNi@NC catalysts: tackling the polysulfide shuttle in Li-S batteries, *Chem. Eng. J.*, 2023, **474**, 145751.

38 J. Liu, S. H. Xiao, Z. Zhang, Y. Chen, Y. Xiang, X. Liu, J. S. Chen and P. Chen, Naturally derived honeycomb-like N,S-codoped hierarchical porous carbon with MS2 (M = Co, Ni) decoration for high-performance Li-S battery, *Nanoscale*, 2020, **12**, 5114–5124.

39 Y. Li, P. Zhou, H. Li, T. Gao, L. Zhou, Y. Zhang, N. Xiao, Z. Xia, L. Wang, Q. Zhang, L. Gu and S. Guo, A freestanding flexible single-atom cobalt-based multifunctional interlayer toward reversible and durable lithium-sulfur batteries, *Small Methods*, 2020, **4**, 1900701.

40 B. Wang, L. Wang, D. Ding, Y. Zhai, F. Wang, Z. Jing, X. Yang, Y. Kong, Y. Qian and L. Xu, Zinc-assisted cobalt ditelluride polyhedra inducing lattice strain to endow efficient adsorption-catalysis for high-energy lithium-sulfur batteries, *Adv. Mater.*, 2022, **34**, 2204403.

41 M. Bi, S. Yao, C. Zhang, H. Yu, X. Zhang, H. Liu, T. Zhang and X. Shen, Hybrid of spinel zinc-cobalt oxide nanospheres combined with nitrogen-containing carbon nanofibers as advanced electrocatalyst for redox reaction in lithium/polysulfides batteries, *Adv. Powder Technol.*, 2022, **33**, 103710.

42 J. Wang, T. Wu, S. Zhang, S. Gu, J. Jin and Z. Wen, Metal-organic-framework-derived N-C-Co film as a shuttle-suppressing interlayer for lithium sulfur battery, *Chem. Eng. J.*, 2018, **334**, 2356–2362.

43 K. Xiao, J. Wang, Z. Chen, Y. Qian, Z. Liu, L. Zhang, X. Chen, J. Liu, X. Fan and Z. X. Shen, Improving polysulfides adsorption and redox kinetics by the Co4N nanoparticle/N-doped carbon composites for lithium-sulfur batteries, *Small*, 2019, **15**, 1901454.

44 K. Wu, Y. Hu, Z. Cheng, P. Pan, M. Zhang, L. Jiang, J. Mao, C. Ni, Y. Zhang, Z. Wang, X. Gu and X. Zhang, Fe3C composite carbon nanofiber interlayer for efficient trapping and conversion of polysulfides in lithium-sulfur batteries, *J. Alloys Compd.*, 2020, **847**, 156443.

45 G. Ruan, Y. Shen, J. Yao, Y. Huang, S. Yang, S. Hu, H. Wang, Y. Fang and X. Cai, Vanadium nitride nanocrystals decorated ultrathin, N-rich and hierarchically porous carbon nanosheets as superior polysulfides mediator for stable lithium-sulfur batteries, *J. Power Sources*, 2023, **566**, 232922.

46 Y. Zuo, Y. Zhu, X. Tang, M. Zhao, P. Ren, W. Su, Y. Tang and Y. Chen, MnO2 supported on acrylic cloth as functional separator for high-performance lithium-sulfur batteries, *J. Power Sources*, 2020, **464**, 228181.

47 D. Liu, C. Zhang, G. Zhou, W. Lv, G. Ling, L. Zhi and Q.-H. Yang, Catalytic effects in lithium-sulfur batteries: promoted sulfur transformation and reduced shuttle effect, *Adv. Sci.*, 2018, **5**, 1700270.

48 D. Wang, Q. Cao, L. Li, B. Jing, Z. Yang, X. Wang, T. Huang, L. Liang, P. Zeng and J. Li, Highly effective trapping-conversion interface based on nickel-modified versatile carbon skeleton enabled high-performance Li-S battery, *ACS Appl. Mater. Interfaces*, 2021, **13**, 16374–16383.

49 L. Chen, Y. Xu, G. Cao, H. M. K. Sari, R. Duan, J. Wang, C. Xie, W. Li and X. Li, Bifunctional catalytic effect of CoSe2 for lithium-sulfur batteries: single doping versus dual doping, *Adv. Funct. Mater.*, 2022, **32**, 2107838.

50 D.-Q. Cai, J.-L. Yang, T. Liu, S.-X. Zhao and G. Cao, Interfaces-dominated Li2S nucleation behavior enabled by heterostructure catalyst for fast kinetics Li-S batteries, *Nano Energy*, 2021, **89**, 106452.

51 S. Yao, C. Zhang, R. Guo, A. Majeed, Y. He, Y. Wang, X. Shen, T. Li and S. Qin, CoS2-decorated cobalt/nitrogen Co-doped carbon nanofiber networks as dual functional electrocatalysts for enhancing electrochemical redox kinetics in lithium-sulfur batteries, *ACS Sustainable Chem. Eng.*, 2020, **8**, 13600–13609.

52 Y. Yang, G. Zheng, S. Misra, J. Nelson, M. F. Toney and Y. Cui, High-capacity micrometer-sized Li_2S particles as cathode materials for advanced rechargeable lithium-ion batteries, *J. Am. Chem. Soc.*, 2012, **134**, 15387–15394.

53 K. B. Celik, E. C. Cengiz, T. Sar, B. Dursun, O. Ozturk, M. Y. Akbas and R. Demir-Cakan, In situ wrapping of tin oxide nanoparticles by bacterial cellulose derived carbon nanofibers and its application as freestanding interlayer in lithium sulfide based lithium-sulfur batteries, *J. Colloid Interface Sci.*, 2018, **530**, 137–145.